Next Materials 11 (2026) 101780

Contents lists available at ScienceDirect

Next Materials

journal homepage: www.sciencedirect.com/journal/next-materials

Research article

Toward the replacement of Nafion®: Innovative PBI-PGO composite membranes as prospective polymer electrolytes for the *"conductivity gap"* range

Matteo Di Virgilio, Matteo Andrea De Luca, Andrea Basso Peressut *, Saverio Latorrata

Politecnico di Milano, Department of Chemistry, Materials and Chemical Engineering "Giulio Natta", Piazza Leonardo da Vinci 32, 20133, Milano, Italy

ARTICLE INFO

Keywords:
Composite membranes
Polybenzimidazole
Phosphonated graphene oxide
Conductivity gap
Anisotropy

ABSTRACT

This work aims at addressing the limitations of Nafion®, the standard polymer electrolyte for Proton Exchange Membrane Fuel Cells, by proposing a set of novel self-assembling PBI-PGO composite membranes capable of sustaining the *"conductivity gap"* temperature range (80–120 °C). Morphological and microstructural analyses (SEM, XRD) highlight uniformity without visible defects and a predominantly amorphous layout. Compositional EDS analysis confirms the presence of all key elements, indicating the successful phosphonation of GO and the subsequent mixing with PBI in various mass proportions. Thermo-mechanical characterization demonstrates the thermal stability of the samples, especially below 120 °C, along with mechanical features in line with those of comparable materials reported in other researches. Electrochemical impedance spectroscopy unveils the effective combination of the thermal resistance of PBI with the water-holding and proton conduction-enhancing properties of PGO, eliminating the need for acid doping. The results recommend the potentiality of the PBI-PGO composite membranes with high PGO content, since PBI-PGO 1:3 provides the highest water retention (257%) combined with an acceptable swelling ratio (26.8%), the best IEC (0.53 meq g^{-1}), and the maximum in-plane (σ_{IP} = 0.087 S cm^{-1}) and through-plane proton conductivities (σ_{TP} = 0.036 S cm^{-1}) at 100 °C.

1. Introduction

In the current years, the prevailing global energy scenario is defined by geopolitical tensions and the interplay within interconnected energy markets [1]. Moreover, the increasing demand for energy as a consequence of population growth has led to a rise in air pollution [2]. Effective strategies should be implemented to contain future problems and fulfill long-term goals related to global warming, as outlined in the Paris Agreement, such as enhancing energy security and controlling emissions [1,3].

In this context, one technology that has emerged thanks to its efficiency and potentially low environmental impacts is the proton exchange membrane fuel cell (PEMFC), which is able to directly convert the chemical energy of a fuel (H_2) into electrical energy via spontaneous redox reactions [4,5].

The most important component of a PEMFC is the proton exchange membrane, with Nafion® serving as the current benchmark material. Nafion® is a specific type of perfluorinated sulfonic acid, known for its excellent properties, but it also has limitations under harsher working conditions (temperature above 80 °C and low hydration), such as loss in mechanical integrity and reduced proton conductivity. Additionally, its high overall cost resulting from the complex manufacturing process (e.g., 0.24 $ cm^{-2} for Nafion® NRE212 [6]) and its classification as a per- and polyfluoroalkyl substance (PFAS) cannot be ignored [7–10]. The latter, in particular, could lead to restrictions to the use of Nafion® by the European Commission, due to the potential release of environmentally persistent perfluorinated compounds during its production and disposal, with risks to human health and ecosystems [11–13].

For these purposes, researchers continue to investigate new materials to overcome perfluorinated membranes, also focusing on those that can operate in high-temperature proton exchange membrane fuel cells (HT-PEMFCs). These high-temperature membranes may offer several advantages, such as good chemical and thermal stability, favorable mechanical properties, low cost, low fuel permeability, and high proton conductivity. A variety of sulfonated polymers have been studied for this purpose, such as sulfonated poly(ether ketone)s (SPEKs), sulfonated

* Corresponding author.
E-mail addresses: matteo.divirgilio@polimi.it (M. Di Virgilio), matteoandrea.deluca@polimi.it (M.A. De Luca), andreastefano.basso@polimi.it (A. Basso Peressut), saverio.latorrata@polimi.it (S. Latorrata).

https://doi.org/10.1016/j.nxmate.2026.101780
Received 21 July 2025; Received in revised form 17 February 2026; Accepted 19 February 2026
Available online 26 February 2026

polysulfones (SPSUs), sulfonated polystyrene copolymers (SPSs), sulfonated polyimides (SPIs), sulfonated poly(p-phenylene)s (SPPs), sulfonated poly(arylene)-type polymers, and sulfonated poly(phosphazene)s (SPPhs) [14–17].

Over the past two decades, a specific material has gained wide attention: polybenzimidazole (PBI), an aromatic linear heterocyclic macromolecule, which exhibits notable resistance to acids and bases, high glass transition temperatures (425–436 °C), and exceptional thermal and mechanical stability, along with insulating properties [18,19]. However, it requires a combination with proton-conducting species due to its low intrinsic proton conductivity, typically through acid doping with phosphoric acid (PA). This process enables interaction with the polymer matrix via the imidazole sites, which work as proton acceptors and facilitate proton mobility [7,20].

Alternative approaches, such as the incorporation of graphene oxide (GO), may increase the proton conductivity, resulting in improved performance, durability, and an extended lifetime of PEMFC systems [21,22]. In particular, the interactions with host polymers through covalent or non-covalent bonds, along with the effective proton transfer capability of GO, are facilitated by the abundant oxygen-containing functional groups (epoxy, hydroxyl, and carbonyl) on its surface and edges [23,24].

The previous characteristics could be improved with the functionalization of GO, as shown with sulfonated graphene oxide (SGO) and phosphonated graphene oxide (PGO) [25–30]. Sulaiman et al. [25] compared the effects of GO, SGO, and PGO (0.25, 0.5, and 1 wt%) on PA-doped PBI under high temperature (> 110 °C) and in anhydrous conditions. The results showed that 0.5 wt% SGO achieved the highest conductivity, followed by 0.5 wt% PGO. Sulfonic acid groups improve hydrogen bonding and support proton transport and water retention in dry environments, owing to their higher acidity, superior to both the ones of phosphonic acid and carboxylic acid groups [25]. Abouzari-Lotf et al. [30] examined the effects of PGO in PA-doped Py-PBI, revealing that a 1.5 wt% inclusion of PGO significantly improves proton conductivity compared to PA-doped Py-PBI. A study by Zhao et al. [28] investigated PGO/PBI blends doped with PA, including a maximum of 2.5 wt% PGO filler, for which a continuous increase in proton conductivity was found. However, these kinds of PA-doped PBI-based membranes exhibit various issues, such as reduced mechanical stability from high acid doping levels, vulnerability to acid leaching in water, the risk of catalyst poisoning, and the difficulty to maintain reasonable proton conductivity values at temperatures higher than 120 °C and up to 160 °C [7,29,31].

In response to the previous limitations, PBI-based composite membranes could be developed to operate between 80 and 120 °C, a range defined as the *"conductivity gap"* in the review of Sun et al. [7]. On one side, this would allow the previously discussed issues of working at temperatures up to 160 °C to be avoided. On the other side, it would enable the possibility to achieve faster reaction kinetics and easier water management with respect to low-temperature PEMFCs (operating below 80 °C), as well as to use a less purified fuel, reducing operational costs [32–34].

In this context, with the aim of avoiding PA doping of PBI, this work delegated proton conduction to PGO only, as proposed in the literature [26,35]. Specifically, composite membranes with PBI to PGO mass ratios of 3:1, 2:1, 1:1, 1:2, and 1:3, which were never examined in the literature, were fabricated by means of a lab-designed solution casting method. The corresponding PGO contents ranged from 25 wt% to 75 wt %, significantly higher than the typical values between 0.5 wt% and 2.5 wt% reported in other researches [25,28,30]). The morphological microstructural, and compositional characteristics of the samples were evaluated using scanning electron microscopy (SEM), energy dispersive X-ray spectroscopy (EDS), X-ray diffraction (XRD), and attenuated total reflection Fourier-transform infrared spectroscopy (ATR-FTIR). Analyses such as thermogravimetry (TGA), water immersion tests, and ion exchange capacity (IEC) evaluation were applied to understand the effects of the different mass ratios on the behavior of the developed materials. In addition, ex-situ electrochemical impedance spectroscopy (EIS) was performed at temperatures of 60, 80, 100, and 120 °C to evaluate proton conductivity in both in-plane and through-plane directions, while tensile tests were conducted to assess the mechanical stability of the samples. The characterization of the produced composite membranes, compared with the benchmark specimens of pure PBI and PGO, offered an understanding of how the interactions among the constituents affected their morphological, thermal, and functional features, thereby confirming the viability and reproducibility of the developed preparation method.

2. Experimental

2.1. Materials

Commercial PBI (Dapozol®) in powdered form was provided by Blue World Technologies Aps (Aalborg, Denmark) with the following characteristics: chemical structure $(C_{20}H_{12}N_4)_n$, a glass transition temperature (T_g) of approximately 425 °C, and a decomposition temperature (T_d) above 600 °C, an average molecular mass of 93,000 g mol^{-1}, and a relative density of 1.30 g cm^{-3} at 23 °C. Graphenea, Inc. (Cambridge, MA, USA) supplied the 0.4 wt% aqueous dispersion of GO with these features: an average particle size of 600 nm, a monolayer content exceeding 95%, and an acidic pH ranging from 2.2 to 2.5. The following chemicals were furnished by Sigma-Aldrich Corporation (St. Louis, MO, USA): concentrated phosphoric acid (H_3PO_4, ACS reagent, purity of 85%), liquid dimethyl sulfoxide (DMSO, chemical structure C_2H_6OS), granules of sodium hydroxide (NaOH, ACS reagent, purity ≥ 97.0%), and sodium chloride (NaCl, ACS reagent, purity ≥ 99.0%). In addition, Durapore® polyvinylidene fluoride (PVDF) filter disks (pore size 22 μm, thickness 125 μm) were purchased from Merck Millipore (Burlington, MA, USA).

2.2. Composite membranes design and preparation

The preparation of novel PBI-PGO composite membranes, defined by mass ratios never analyzed in the literature, was founded on a solution casting method already used in previous works [9,36] and encompassed a new GO phosphonation process derived from other laboratory studies [30,37]. The entire process developed in this work is summarized in Fig. 2.1.

The first step (1) involves the refinement of the PBI powder by grinding in an agate mortar, followed by dissolution at a 2 wt% concentration in DMSO for 2 h at 100 °C (± 2 °C) under magnetic stirring. In the second step (2), the phosphonation of GO was carried out by replicating a different functionalization adopted elsewhere [21,27]: H_3PO_4 was added to the ultrasonicated (15 min) aqueous dispersion of GO (with an H_3PO_4-to-GO molar ratio of 10), and magnetic stirring was applied for 3 h at 25 °C (± 2 °C), then continued for an additional 3 h at 100 °C (± 2 °C). In step (3), vacuum filtration was applied to PGO for 2 h with a PVDF filter disk placed in a Büchner funnel, in order to recover a paste. During this phase, a dilution with 300 mL of deionized water was exploited to increase pH for safety reasons. Then, the paste-like compound was dried at 40 °C in an oven to eliminate residual water. The next step (4) involved incorporating 1 wt% of PGO into DMSO by subjecting them to magnetic stirring for 3 h, followed by 45 min of ultrasonication. To prepare the PBI-PGO composite membranes in step (5), the two solutions of PBI and PGO in DMSO were blended for 3 h with vigorous stirring at room temperature.

Finally, to support the self-assembly of the membranes, the PBI-PGO solution was cast into a 7 cm Petri dish and oven-dried at 90 °C for 3–5 h (step (6)). This operating temperature was chosen to prevent the potential thermal reduction of the PGO sheets [38]. In addition, pure PBI and virgin PGO membranes were prepared and characterized to serve as benchmarks, guaranteeing a comparative analysis. The production of

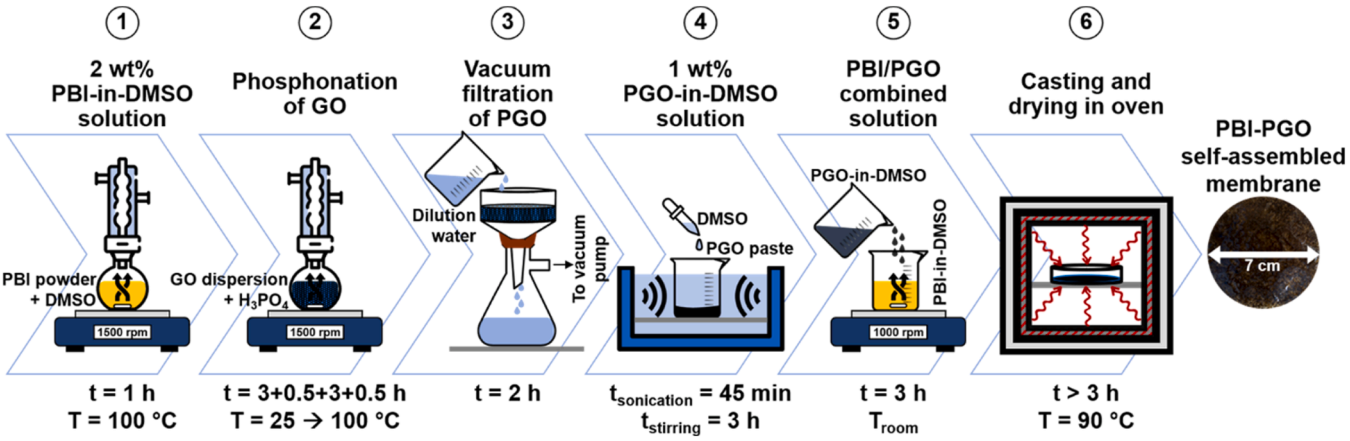

Fig. 2.1. Process scheme for the preparation of PBI-PGO composite membranes.

the former involved dissolving the PBI powder in DMSO (step (1)), then casting and drying in an oven for 3 h (step (6)). In contrast, the preparation of pure PGO required steps (2) and (3), followed by drying the PGO deposit, recovered from the Büchner funnel, at 40 °C for a few hours to remove residual water and allow the completion of the self-assembly of the membrane.

In this work, instead of using PGO as a filler [28,30], the mass ratios of PBI to PGO ranged from 3:1 (with a minimum of 25 wt% PGO) to 1:3 (with a maximum of 75 wt% PGO) through intermediate ratios of 2:1, 1:1, and 1:2 (Table 2.1). The as-fabricated composite membranes were labeled PBI-PGO A:B, where A denotes the PBI mass content and B refers to the PGO mass content. Moreover, the total mass of the constituents was set at 0.25 g to attempt control over the final thicknesses of the products.

2.3. Morphological and microstructural characterization

2.3.1. Scanning electron microscopy (SEM)

Scanning electron microscopy (SEM) images of the membranes surface (5000x magnification) and cross-section (1000x magnification) were acquired using an EVO 50 EP device by ZEISS AG (Oberkochen, Germany) under the following operating conditions: chamber pressure of 9.6×10^{-5} Pa, accelerating voltage of 5 kV, and a maximum probe current of 70 μA. Moreover, the preliminary preparation required mounting the membrane sample on a holder with dual-sided carbon tape and sputter-coating it with a 20 nm gold film.

2.3.2. X-ray diffraction

To verify the crystallinity or amorphous nature of the samples, X-ray diffraction analysis was performed using the Rigaku SmartLab SE diffractometer (Tokyo, Japan). The system employed a copper filament that generated K-α radiation with a wavelength of 1.54 Å, operating within an angular range of $5° < 2\theta < 30°$, with a step size of 0.02° and a scanning speed of 1° min^{-1}.

2.4. Compositional characterization

2.4.1. Fourier-transform infrared spectroscopy

Fourier-Transform Infrared Spectroscopy (FTIR) under Attenuated Total Reflection (ATR) was executed on the composite membranes by employing a Thermo Nicolet iN10 MX spectrometer provided by Thermo Fisher Scientific Inc. (Rodano, Italy). The setup consisted of a single reflection silicon crystal and a liquid nitrogen (LN_2)-cooled mercury cadmium telluride (MCT) detector. The measurements were carried out over a wavenumbers range of 4000–650 cm^{-1}, with 128 scans and a resolution of 4 cm^{-1}.

2.4.2. Energy dispersive X-ray spectroscopy

Energy dispersive X-ray spectroscopy (EDS) was conducted using a ZEISS AG EVO 50 EP scanning electron microscope and an Oxford Instruments INCA200 PENTAFETLZ4 EDX spectrometer at 500x magnification across different areas of each sample. The operational conditions were set to 20 kV of acceleration voltage, 100 pA of maximum probe current, and 30–40 Pa of pressure range.

2.5. Thermo-mechanical characterization

2.5.1. Thermogravimetric analysis

The TGA Q500 (TA Instruments, New Castle, DE, USA) was used to evaluate the thermal properties of the membranes by means of a constant heating rate of 10 °C min^{-1} between 30 and 800 °C, under a flux of 55 mL min^{-1} of pure nitrogen. An electronic microbalance was used to determine the residual mass percentage as a function of temperature, allowing the identification of modifications in the materials.

2.5.2. Mechanical testing

The mechanical properties of the PBI-PGO A:B composite membrane were inspected through tensile tests at a strain rate of 1 mm min^{-1}, executed via the Synergie 200 test system by MTS Systems Corporation (Eden Prairie, MN, USA) on four rectangular specimens (7 cm×1 cm) for each formulation.

Table 2.1
Amounts of PBI, PGO, and their respective solutions used in preparing PBI-PGO A:B samples.

	PBI-PGO 3:1	PBI-PGO 2:1	PBI-PGO 1:1	PBI-PGO 1:2	PBI-PGO 1:3
PBI mass (g)	0.188	0.167	0.125	0.083	0.063
PBI-in-DMSO solution mass (g)	9.375	8.333	6.250	4.167	3.125
PGO mass (g)	0.063	0.083	0.125	0.167	0.188
PGO-in-DMSO solution mass (g)	6.250	8.333	3.125	16.67	18.75

2.6. Functional and electrochemical characterization

2.6.1. Ion exchange capacity

Acid-base back-titration was used to evaluate the Ion Exchange Capacity (IEC) [39,40]. The process started with the drying in vented oven (60 °C, 1 h) of three specimens for each composite membrane and the subsequent measurement of the dry masses. Each sample was equilibrated for 48 h in a 2 M NaCl aqueous solution at room temperature. Then, the solution was titrated with a 0.01 M NaOH solution (pH = 12) at room temperature under magnetic stirring (800 rpm), and the stabilized pH was repeatedly measured at each addition using a FiveEasy™ pH/mV meter by Mettler Toledo (Columbus, OH, USA). The IEC values (meq g^{-1}) were determined using Eq. (2.1), where m_{dry} (g) represents the mass of the dried sample, C_{NaOH} (mmol mL^{-1}) is the concentration of the titrant solution, and V_{NaOH} (mL) is the NaOH volume at the turning point of the V_{NaOH}–pH titration curve:

$$IEC\ (meq\ g^{-1}) = \frac{V_{NaOH} \cdot C_{NaOH}}{m_{dry}} \tag{2.1}$$

2.6.2. Water immersion tests

The capacity to retain water and the durability of the composite membranes in a water-rich environment were studied over a period of 3 months through a lab-designed water immersion test. The first step consisted of drying the samples in the vented oven for 2 h at 60 °C to eliminate any moisture and determine their dry mass (m_{dry}, g). Then, each specimen was submerged in a separate beaker with 200 mL of deionized water and sealed with parafilm tape. During the entire test, wet mass values (m_{wet}, g) were measured after 2, 7, 14, 30, 60, and 90 days. The procedure consisted of removing the samples from the beaker, using a paper towel to eliminate excess water from the surface, and recording the m_{wet} values with an analytical balance. Using Eq. (2.2) [41], the percentage mass increase (MI) was obtained:

$$MI\ (\%) = \frac{m_{wet} - m_{dry}}{m_{dry}} \cdot 100 \tag{2.2}$$

Similarly, Eq. (2.3) was used to obtain the long-term swelling ratio, a numerical value indicating the tendency to swell upon water sorption, which should be minimal to avoid the possibility of mechanical damage in a fuel cell assembly. A Fujisan Digital micrometer (0–25 mm, ± 1 μm) served to measure the initial dry thickness (t_{in}, μm) and the final thickness at the end of the tests (t_{fin}, μm), which were then used to determine the swelling ratio (SR) [41]:

$$SR\ (\%) = \frac{t_{fin} - t_{in}}{t_{in}} \cdot 100 \tag{2.3}$$

2.6.3. Electrochemical impedance spectroscopy

Electrochemical impedance spectroscopy (EIS) was conducted to evaluate the ex-situ proton conductivity of the PBI-PGO A:B composite membranes in a lab-designed insulated humid chamber at 60, 80, 100, and 120 °C under 95% RH. Prior to the test, three rectangular samples of each formulation (3.5 cm length x 1.0 cm width) were dried for 2 h at 60 °C to obtain their dry thickness. They were then anchored to an inert Teflon® cell with two stainless steel electrodes and placed in the chamber filled with 600 mL of deionized water for 1 h at the specific test temperature. The latter was controlled by a thermocouple positioned directly in the chamber and by the circulation of heated oil into its external shell. After 1 h, the STEMlab™ 125–14 by Red Pitaya (Solkan, Slovenia) was connected to an interface laptop, then to a resistive element, and finally to the cell electrodes using the required cables and clips to complete the circuit. EIS tests were performed in the frequency range of 1–10^7 Hz. The results were acquired in the form of Bode diagrams, which were then converted into Nyquist plots and analyzed using the ZView® 3.0 software (Scribner Associates Inc., Southern Pines, NC, USA) to determine the average values of the internal resistance (R_i, Ω) with an appropriate equivalent circuit [42].

Two *ad-hoc* Teflon® cell configurations (Fig. 2.2) were adopted to evaluate both in-plane conductivity (σ_{IP}) and through-plane conductivity (σ_{TP}) values (S cm^{-1}). For the former configuration, Eq. (2.4) was used to calculate the final outcome, where d_1 (cm) represents the distance between the electrodes, while w_1 (cm) and t (cm) denote the width and dry thickness of the sample, respectively. For the latter configuration, Eq. (2.5) was applied to extrapolate the through-plane performance, where the product $w_2 \cdot d_2$ (cm^2) defines the contact area of the electrodes:

$$\sigma_{IP} = \frac{1}{\rho_{IP}} = \frac{d_1}{R_i \cdot w_1 \cdot t} \tag{2.4}$$

$$\sigma_{TP} = \frac{1}{\rho_{TP}} = \frac{t}{R_i \cdot w_2 \cdot d_2} \tag{2.5}$$

Either way, the activation energy (E_a, kJ mol^{-1}) of proton transfer was deduced from the linearized variant of the Arrhenius-type law, clarified in Eq. (2.6) through parameters such as the working temperature T (K), the universal gas constant R (J (mol K)$^{-1}$), and the pre-

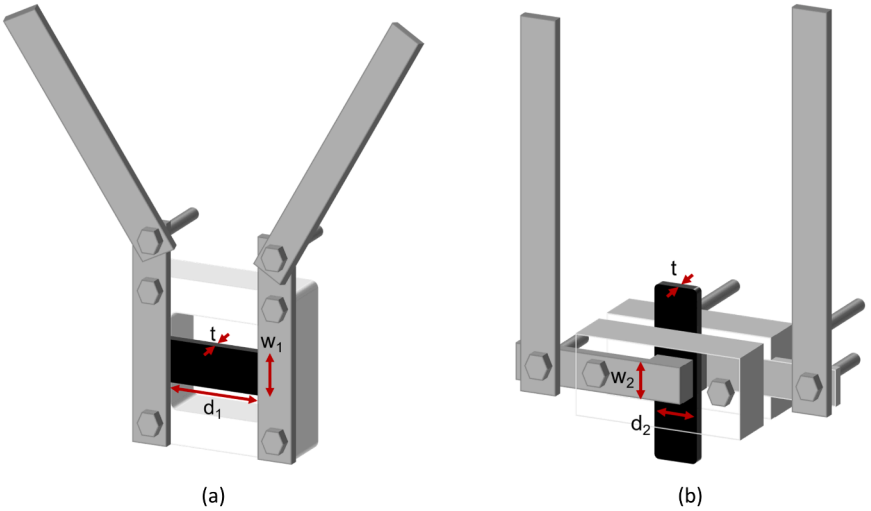

Fig. 2.2. Three-dimensional rendering of (a) in-plane and (b) through-plane Teflon® cell configurations. Reprinted from Journal of Science: Advanced Materials and Devices, 9 (3), M. Di Virgilio, A. Basso Peressut, S. Provato, S. Latorrata, Development and characterization of novel PBI/SGO composites as possible proton exchange membranes filling the *"conductivity gap"*, 1–12, Copyright (2024), with permission from Elsevier.

exponential factor σ_0 (S K cm^{-1}) [28,30].

$$\ln(\sigma \cdot T) = \ln(\sigma_0) - \left(\frac{E_a}{R}\right) \cdot \left(\frac{1000}{T}\right) \quad (2.6)$$

Furthermore, the dimensionless anisotropy factor (AF), determined using Eq. (2.7) according to the approach of Luo et al. [43], was employed to examine the correlation between the in-plane and through-plane proton conductivities of the PBI-PGO A:B composite membranes. This evaluation aimed to determine whether proton transport within the membranes is more favorable in one direction than the other:

$$AF = \frac{\sigma_{IP} - \sigma_{TP}}{\sigma_{IP} + \sigma_{TP}} \quad (2.7)$$

3. Results and discussion

Considering that the primary purpose of this work was to combine PBI and PGO to form composite membranes featuring mass ratios never explored in the literature, the study investigated relative proportions ranging from 3:1, i.e., a minimum PGO content of 25 wt%, to 1:3, indicating a maximum PGO content of 75 wt%. Moreover, the workflow, similar to the one employed in a previous work by the authors on PBI-SGO analogues [9], was designed to be safe, cost-effective, and reliable. Another key innovation of this research lied in the preparation and use of phosphonated graphene oxide, which was developed following the same procedure described by Basso Peressut et al. [27] for the production of sulfonated graphene oxide (SGO). This approach exploited the ability of GO to be functionalized by acidic substances, in this case phosphoric acid, a triprotic acid which could be able to enrich the substrate with functional groups characterized by two mobile protons. As verified in previous works, DMSO proved to be an effective solvent for both PBI and functionalized GO. Thanks to its non-toxicity, it was also suitable for this study, allowing the preparation of homogeneous solutions of PBI and PGO in DMSO [9,44,45]. The thicknesses of PBI-PGO A:B membranes, reported in Table 3.1, were in the order of several tens of micrometers. The composite membranes with higher PGO contents exhibited lower values, closer to those of the pristine membrane, despite a fixed total mass of constituents, probably due to the superior contribution of the PGO packing ability. However, the average outcomes remained comparable to the ones of commercial membranes and in agreement with other findings reported in the literature [9,30,36,46].

Fig. 3.1 (top row) shows the macroscopic appearance of the produced composite membranes. The PBI-PGO 3:1 sample appeared more yellowish and transparent, approaching the typical features of unmodified PBI [9,29,47], along with dark aggregates ascribable to PGO segregation. As the PGO content increased, a color gradient became evident among the sample. When the PGO amount reached 66.7 wt% (PBI-PGO 1:2) and 75 wt% (PBI-PGO 1:3) of the total composition, the partial loss of transparency was juxtaposed to a more homogeneous texture.

In addition, as visible from the images in the bottom row of Fig. 3.1, the composite membranes exhibited a decent foldability, a characteristic that was not checked in previous works about comparable materials reported in [9,36]. However, a qualitatively greater difficulty in handling was observed at higher PGO contents.

3.1. Morphological and microstructural characterization

3.1.1. Scanning electron microscopy

Fig. 3.2 displays the surface SEM images at 5000x magnification of PBI-PGO A:B composite membranes, pristine PBI, and virgin PGO. The samples (Figure 3.2**b-f**) did not exhibit visible defects or flaws, thus a good overall homogeneity. In particular, higher amounts of PBI involved a flatter and smoother surface similar to that of the pure polymer (Figure 3.2**a**), as well reported in the literature [47,48]. Conversely, the composite membranes with larger PGO content showed a more undulated surface, probably due to a combination of π-π stacking interactions, among the π-conjugated PBI chains and the sp^2-hybridized regions of PGO, and a favored hydrogen bonding, among the basic sites of the polymer and the oxygen-containing functionalities on the PGO portion [25,45,47]. The growing concentration of the latter could further influence surface features by causing tensions within the structural network [49].

In Fig. 3.3**b-c**, PBI-PGO 3:1 and PBI-PGO 2:1 membranes displayed a compact and homogeneous cross-section, comparable to the one of PBI (Fig. 3.3**a**), without signs of a stratified arrangement. The rise of PGO amount over 50 wt% brought to a more visible stratification due to the stacking of prevailing PGO layers, similarly to the pure PGO cross-sectional image (Fig. 3.3**g**) [50]. Nevertheless, the overall structure remained compact and undamaged.

3.1.2. X-ray diffraction

X-ray diffractograms of the as-prepared composite membranes and relative benchmarks are shown in Fig. 3.4. For the former ones, predominantly amorphous microstructures were presumed, similar to the one of virgin PBI. Indeed, a broad band attributed to the PBI fraction arose between 20° and 30°. It may denote the convolution of an amorphous region with a semi-crystalline one, resulting from the wrapping of facing chains [28,51,52]. With increasing PGO amount, the intensity of such a band tended to weaken, likely due to PGO interfering with the stacking of PBI chains [28]. In parallel, a reflection started to appear between 5° and 15°, probably correlated to the PGO moieties. As confirmation, the diffractogram of pure PGO was characterized by a sharper peak at $2\theta \approx 9.2°$, remarking its crystallinity. The comparison of the evaluated interplanar distance (d = 0.96 nm from Bragg's law [36]) with that of pure GO ($2\theta = 10.8°$, d = 0.82 nm [27,36,53,54]) clearly indicated that phosphonation caused a shift to lower diffraction angles. This shift could be ascribed to an increase in the interlayer spacing due to the steric hindrance of phosphonic acid groups (–PO_3H_2) alongside pre-existing oxygen functionalities (such as epoxy, hydroxyl, and carboxyl groups). Dissimilarly, the contributions detected in all PBI-PGO A:B composite membranes were much broader compared to pristine PGO. Consequently, amorphous traits were appreciated even at 75 wt% PGO content, as also suggested by the slight transparency commented in Section 2.3. Several factors could likely participate in this specific behavior, such as the significant exfoliation and random distribution of PGO sheets during the solution casting procedure. In the worst case, a slight reduction of the original GO layers could be hypothesized. As observed in a previous study, the main elements that were supposed to be responsible for this were an aftereffect of the acid functionalization of GO and the dissolution step in DMSO [9,55,56]. Nonetheless, a satisfactory blending of the two species up to an effective self-assembly process could be validated by the recognition of bands associated with both constituents, regardless of the PBI to PGO mass ratio. Moreover, proton transport is known to be facilitated when long-range disorder and the absence of regular atomic arrangement predominate, as in this case,

Table 3.1
Average thicknesses of the PBI-PGO A:B composite membranes, pure PBI, and pure PGO.

	PBI	PBI-PGO 3:1	PBI-PGO 2:1	PBI-PGO 1:1	PBI-PGO 1:2	PBI-PGO 1:3	PGO
Thickness (μm)	58 ± 7.0	59 ± 13	53 ± 17	45 ± 3.3	29 ± 7.3	23 ± 5.5	15 ± 3.0

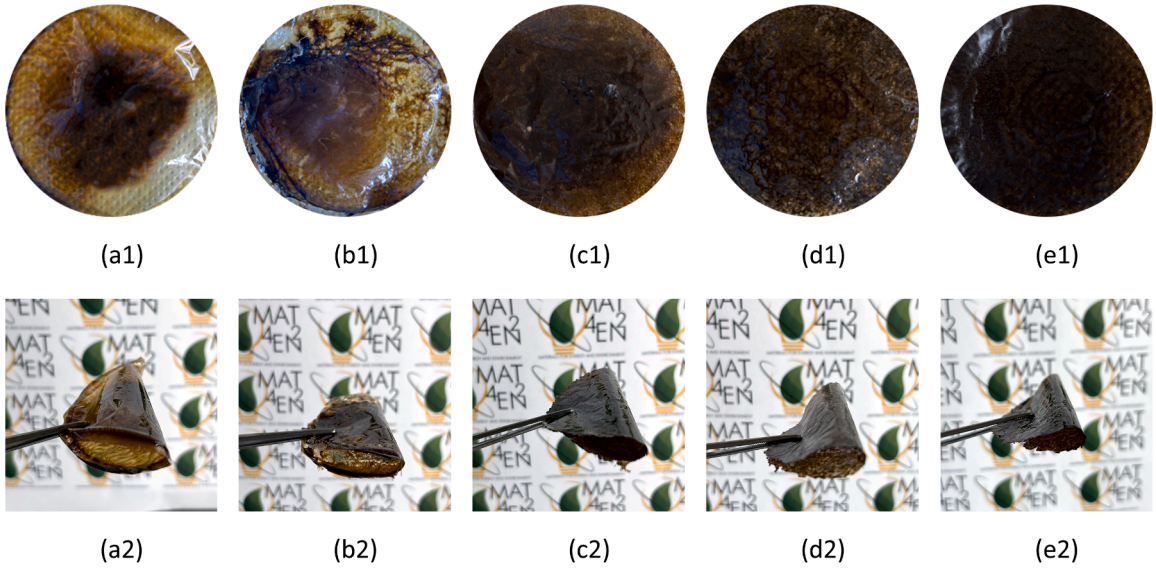

Fig. 3.1. Macroscopic overviews of the PBI-PGO composite membranes at mass ratios (a1) 3:1, (b1) 2:1, (c1) 1:1, (d1) 1:2, (e1) 1:3, with the corresponding cross-sections (a2-e2) in a bent form.

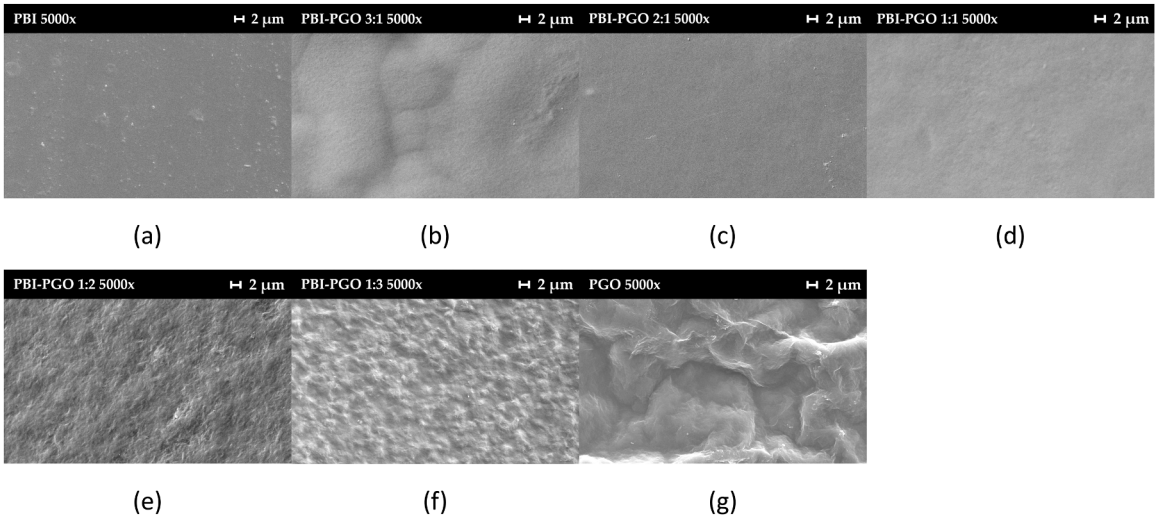

Fig. 3.2. 5000× magnified SEM surface views of specimens: (a) PBI, (b-f) PBI-PGO A:B, and (g) PGO.

where the manufactured samples showed a mainly amorphous nature [28].

3.2. Compositional characterization

3.2.1. Fourier-transform infrared spectroscopy

The ATR-FTIR spectra of the PBI-PGO A:B composite membranes (Fig. 3.5**b**) featured a resemblance to the pure PBI spectrum. In detail, the contribution (a) at 3400 cm^{-1} [57] corresponded to the stretching of free N–H groups not involved in hydrogen bonding, while the broad band (b) at 3100 cm^{-1} may be related to the combination of the stretching vibrations of self-associated N–H and –OH functionalities [25,58]. Three signals associated with C═N, C═C, and ring vibrations, characteristic of the conjugation between benzene and imidazole rings in the PBI structure, were assigned to wavenumbers (c) 1629, 1610, and 1590 cm^{-1}, respectively [59,60]. Other typical peaks were observed at (d) 1532 cm^{-1} (in-plane deformation of benzimidazole), (e) 1438 cm^{-1} (in-plane vibration of 2,6-disubstituted benzimidazole), (f) 1280 cm^{-1} (C–N stretching vibrations in the imidazole moieties), and (g) 1012 cm^{-1} (benzene ring vibration) [57,59,61].

Some variations emerged in the composite membranes along with the growth of the included PGO amount, loosely indicating both the proper functionalization of GO and the correct combination of PBI and PGO. The reshaping of the broad bands at 3400–3100 cm^{-1} could be attributed to potential hydrogen bonding and acid-base interactions among the PBI and PGO fractions [25,60], which diminished the polymer-polymer interplay. Conversely, an incremental attenuation of the characteristic bands of PBI, especially the (c), (e), and (f) ones, was coherent with the PBI amount decreasing from 75 wt% to 25 wt%. Nevertheless, the reciprocal interference and overlapping of the characteristic bands of PGO and PBI made the contributions of the former less distinguishable in the spectra of the composite membranes. Indeed, the phosphonated derivative (Fig. 3.5**a**) distinctly displayed a series of vibrational bands attributable to both the GO structure and the introduced functional groups. The broad band (h), between 3700 and 2800 cm^{-1}, represented the overlap of several vibrations, including the –OH stretching of hydrophilic functionalities (hydroxyl and carboxylic acid groups) and adsorbed water molecules [12,25,27]. The peaks (i) at

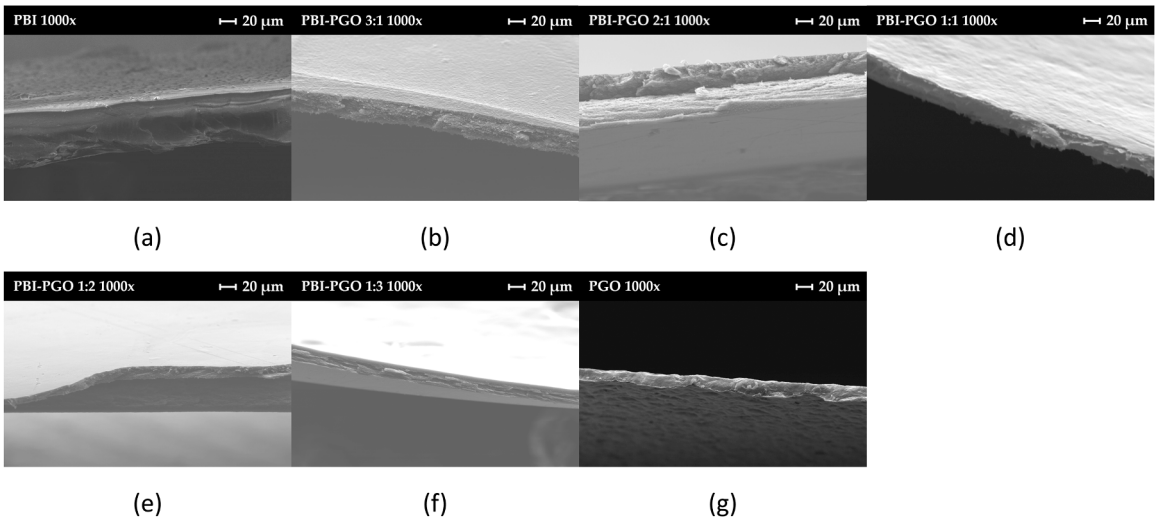

Fig. 3.3. Cross-sectional SEM views of specimens at 1000× magnification: (a) PBI, (b-f) PBI-PGO A:B, and (g) PGO.

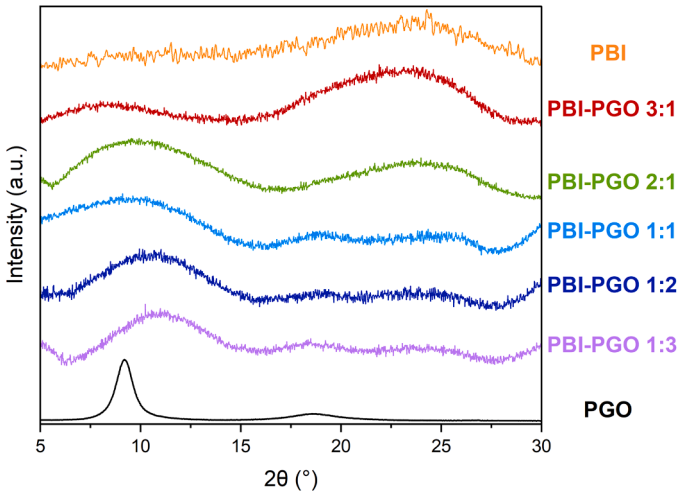

Fig. 3.4. XRD patterns of the PBI-PGO A:B composite membranes, pure PBI, and pristine PGO.

1810 cm^{-1}, (j) at 1715 cm^{-1}, and (k) at 1618 cm^{-1} likely referred to the C═O stretching in anhydride groups, the C═O stretching of carboxyl and carbonyl groups, and the O–H bending in adsorbed water, respectively [28,50]. Moreover, the functionalization of GO was probably assessed by the following contributions: the small peak (m) at 1220 cm^{-1} (stretching of the P═O bonds), the less intense peak (l) at 1374 cm^{-1} (removal of peripheral carboxylic groups in favor of phosphonic acid ones), the small band (n) at 1050 cm^{-1} (symmetric stretching of P–OH bonds and vibration of C–P covalent bonds), and the band (o) at 970 cm^{-1} (asymmetric OH–P–OH stretching) [25,28]. The latter two vaguely appeared as weak shoulders in the spectra of PBI-PGO 1:2 and PBI-PGO 1:3.

3.2.2. *Energy dispersive X-ray spectroscopy*

Energy dispersive X-ray spectroscopy (EDS) provided semi-quantitative information about the composition of the composite membranes (Fig. 3.6**a**). The proper combination of PBI and PGO, previously suggested by other techniques, was corroborated by the mass concentrations of carbon, nitrogen (a characteristic element of PBI), oxygen (indicating the presence of GO moieties), and phosphorus (demonstrating the successful functionalization) in all prepared PBI-PGO A:B samples. The increasing phosphorus content from the PGO

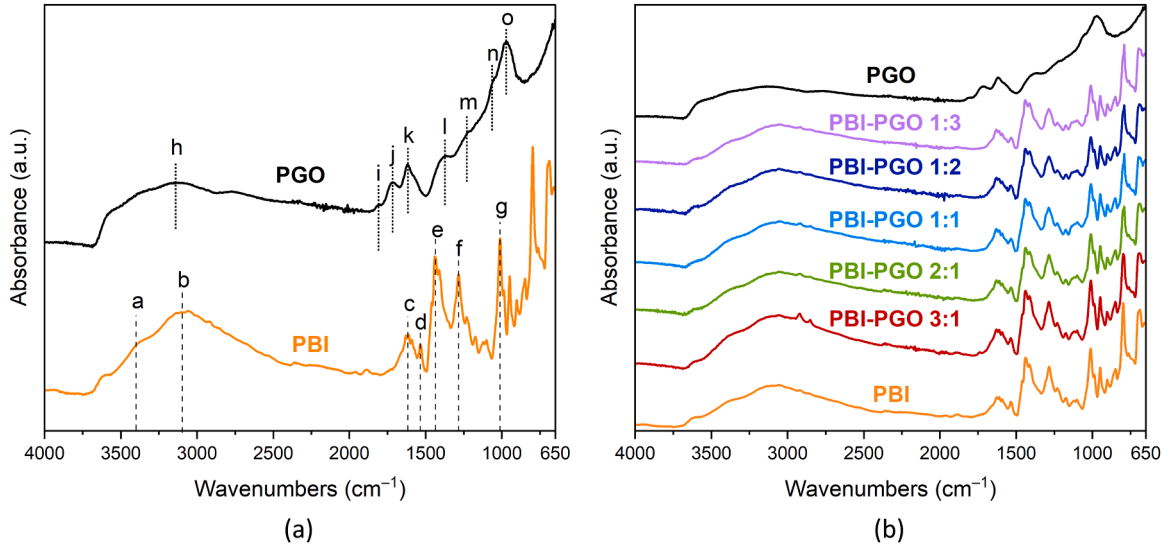

Fig. 3.5. ATR-FTIR spectra of (a) reference PBI and PGO; (b) Comparison of the ATR-FTIR spectra of all PBI-PGO A:B samples and the benchmark materials.

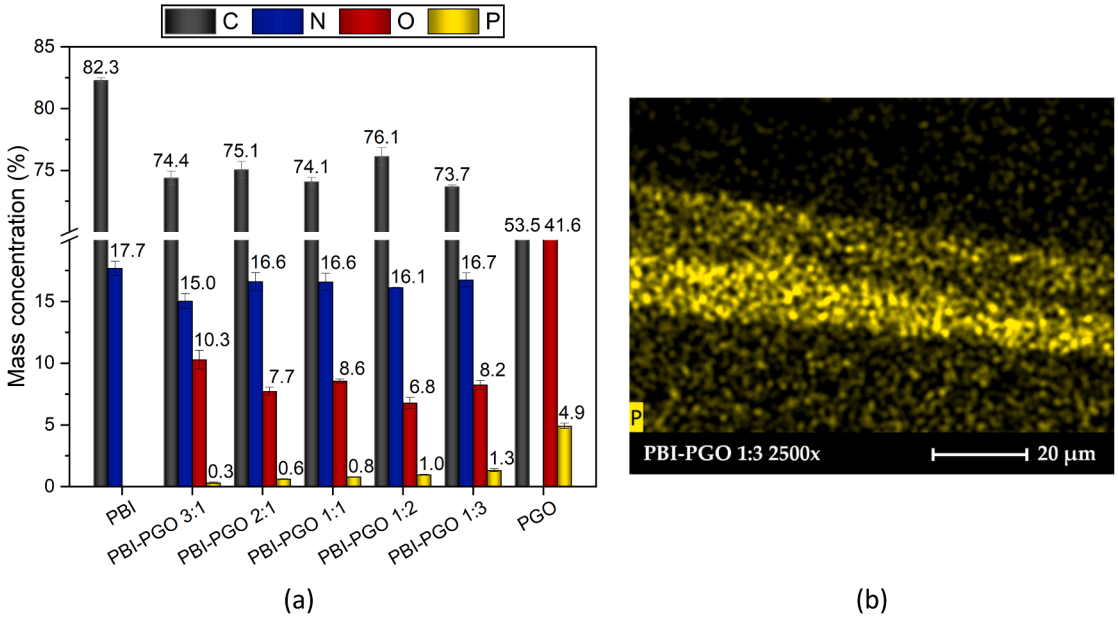

Fig. 3.6. (a) EDS compositional analysis of all studied membranes; (b) Cross-sectional distribution of phosphorus in PBI-PGO 1:3.

portion, up to 1.3 ± 0.2% in PBI-PGO 1:3, further highlighted its conservation during the preparation phase. In contrast, the oxygen trend appeared irregular, despite the insertion of phosphonic acid groups onto the original GO framework. This outcome could likely be due to a very partial loss of oxygen-containing groups from GO during the fabrication method [55,56,62]. A qualitative cross-sectional EDS analysis confirmed the spatial homogeneity of all elements. Within this context, a representative image of the adequate distribution of phosphorus across the thickness of PBI-PGO 1:3 is included in Fig. 3.6**b**.

3.3. Thermo-mechanical characterization

3.3.1. Thermogravimetric analysis

The thermograms of the PBI-PGO A:B, pure PBI, and pure PGO membranes, collected in Fig. 3.7, illustrated a five-stage, four-stage, and two-stage mass loss, respectively. The first mass loss (blue band) around

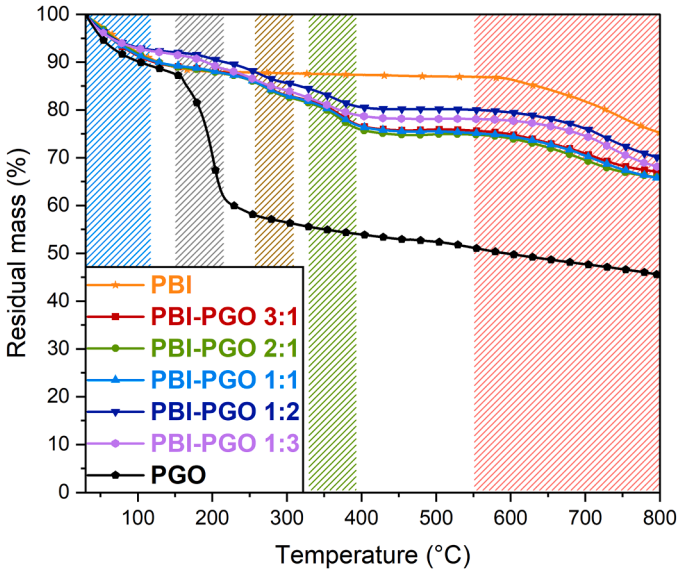

Fig. 3.7. Thermogravimetric curves of the PBI-PGO A:B composite membranes, reference PBI, virgin and PGO.

100 °C was primarily associated with the removal of trapped moisture [28,36], which was common for all samples. The retention of the composite membranes (7.9%) was better than pure PGO (9.8%), thanks to the thermal stability imparted by the PBI chains. Notably, the remaining mass was greater than 92% within the *"conductivity gap"* temperature range (80–120 °C), with losses not ascribable to the molecular structure of the prepared materials. The degradation of oxygen-containing functional groups took place during the second stage (grey band), occurring between 150 and 230 °C, more markedly in the pure PGO sample [25, 28]. On the contrary, PBI was unaffected in the same range, since it does not contain oxygenated moieties, as confirmed by EDS results (**Section 3.2.2**) [37]. The composite membranes revealed a mass drop of ≈ 2%, which is one order of magnitude lower than that of pure PGO (17%), highlighting a good thermal stability, probably derived from hydrogen bonding interactions, as well suggested by ATR-FTIR spectra, that stabilized the oxygenated moieties of PGO. The third mass loss (dark yellow band) was probably related to the decomposition of phosphorus-containing functionalities (between 250 and 300 °C), confirming the correct modification of GO and the incorporation of the phosphonated variant in the fabricated materials [25]. A delayed removal of strongly bound oxygen-bearing groups could be also conceived as a consequence of the thermal resistance conferred by the phosphonic acid groups [25,30,35]. The further decrease in residual mass (green band), occurred between 300 and 380 °C (4.5–5.5%), could result from the partial destruction of the –NH– and –N═groups in the imidazole rings of PBI [25,63]. Peculiarly, the corresponding mass drop was practically indistinguishable in pure PBI, suggesting that the major contribution to this loss came from a disturbance provoked by the interaction with PGO [36]. The last thermal event (red band) affecting the composite membranes started around 550 °C and provoked a mass loss of 8.5–10%, primarily because of the breakdown of the PGO structure (5.5% mass loss in the pure sample) and the degradation of the carbonaceous PBI backbone chains (12% mass loss in the pure sample) after 600 °C [36,37,64]. At the end of the test (800 °C), all composite membranes showed better thermal stability than PGO thanks to the presence of PBI moieties. Indeed, the residual mass of more than 65%, fairly consistent regardless of the employed PBI to PGO mass ratio and in the proximity of the value reached by the pure polymer, was higher with respect to the one of pure PGO (46%). Overall, the best outcome was obtained by PBI-PGO 1:2 (around 70% of retained mass), with a value of

Table 3.2
Average tensile test data (peak stress, maximum strain, and Young's modulus) for PBI-PGO A:B samples in comparison to pure PBI.

	PBI	PBI-PGO 3:1	PBI-PGO 2:1	PBI-PGO 1:1	PBI-PGO 1:2	PBI-PGO 1:3
Peak stress (MPa)	23.0 ± 6.59	26.7 ± 4.67	25.6 ± 8.27	16.6 ± 6.74	27.6 ± 12.18	14.6 ± 4.90
Maximum strain (%)	19.8 ± 8.38	6.63 ± 2.53	3.36 ± 0.89	1.46 ± 0.80	3.67 ± 1.29	1.36 ± 1.28
Young's modulus (GPa)	0.92 ± 0.33	2.42 ± 0.64	1.57 ± 0.23	1.69 ± 0.32	3.40 ± 0.53	2.20 ± 0.39

92% within the *"conductivity gap"*.

3.3.2. Mechanical Testing

The average peak stresses (PS), maximum strains (MS), and Young's moduli (YM), deduced from the mechanical tests executed on the PBI-PGO A:B composite membranes and pure PBI, are reported in Table 3.2. A decrease in maximum strain was implicated by gradually higher PGO contents, i.e., from 6.6 ± 2.5% of PBI-PGO 3:1 to 1.4 ± 1.3% of PBI-PGO 1:3, identifying a more rigid behavior typically associated with the characteristics of GO-based materials and the handling challenges mentioned in Section 3. PBI-PGO 1:2 represented an exception, since it displayed an elongation at break of 3.7 ± 1.3%. However, the relatively low values of maximum strain observed for the PBI-PGO A:B samples could also be linked to the generation of micro-defects during the trimming process of the strips from the as-prepared membranes, which might have acted as points of stress concentration during tensile tests.

Differently, the combination with PGO was beneficial from the perspective of tensile strength and Young's modulus, both enhanced with concentrations up to 66.7 wt% if compared with virgin PBI (PS of 23.0 ± 6.6 MPa, YM of 0.92 ± 0.33 GPa). Indeed, PBI-PGO 1:2 (PS of 27.6 ± 12.2 MPa, YM of 3.40 ± 0.39 GPa) was again the best performing formulation, thanks to a 20% and 270% increase of the two properties, respectively. This outcome underlined the reinforcing action promoted by GO and its derivatives, elucidated by the ability to elevate interfacial adhesion via hydrogen bonding and acid-base interactions on the multitude of functional groups decorating their structure [28,50,52].

3.4. Functional and electrochemical characterization

3.4.1. Ion exchange capacity

Table 3.3 presents the average ion exchange capacity (IEC) values for the PBI-PGO A:B composite membranes, pure PBI (from a previous work [36]), and pure PGO. The adequate reciprocal mixing and coexistence of PBI and PGO could be confirmed by the IEC trend. Beginning with a PBI-PGO mass ratio of 3:1, an IEC value of 0.160 ± 0.031 meq g^{-1} was obtained, marking an increase of 67% over that of pure PBI. Afterwards, the propensity to ion exchange reached the highest value of 0.532 ± 0.152 meq g^{-1} at the largest PGO content, i.e., at the PBI-PGO 1:3 mass ratio, corresponding to an increase of 454% with respect to the pure polymer. This increasing trend with progressively higher PGO content can be explained by the properties of PGO, which contains functional groups proton to proton displacement, such as carboxyl (–COOH), hydroxyl (–OH), and phosphonic acid ($–PO_3H_2$) ones [30,35]. In contrast, PBI showed a quite low ion exchange capacity, possibly deriving from the limited presence of mobile protons within its molecular structure.

Nevertheless, the results of the PBI-PGO A:B composite membranes were oddly lower than those of the PBI-GO samples studied in a previous work, which achieved a maximum of 0.803 meq g^{-1} [36]. The unwanted partial reduction of GO during the PBI-PGO production process, which led to the loss of labile yet useful oxygenated functional groups [55,56], could be presumed in conjunction with the XRD patterns (Section 3.1.2). Alternative explanations for the surveyed IEC values could include the formation of acid-base interactions between benzimidazole and phosphonic groups or the self-condensation of PGO moieties within the composite membranes. These interactions may block some protons (H^+) within the phosphonic acid groups, limiting their availability for the direct exchange with sodium ions (Na^+), thus preventing a realistic detection during the IEC tests.

3.4.2. Water immersion tests

The percentage mass increases after water immersion tests of the PBI-PGO A:B composite membranes, pure PBI, and benchmark PGO are shown in Fig. 3.8**a**. PBI-PGO specimens and pure PBI ensured an exceptional resistance to the aqueous environment, which may be attributed to the remarkable structural stability of PBI [18,32]. In contrast, PGO degraded after just few hours, likely due to weaker intermolecular bonds compared to PBI and a strong influence of its hydrophilic functionalities, which formed more hydrogen bonds and induced a pronounced proneness to penetration and sorption of water molecules. The resulting expansion induced internal stresses, eventually compromising the stability of the material and leading to its disintegration. Such an issue was positively tackled by the blending with PBI, which guaranteed a robust response to all composite membranes, independently from the mass ratio of constituents. For the sample including the highest amount of PBI (PBI-PGO 3:1), the curve tended to approach saturation after 30 days, whereas the same occurred after 60 days or more at higher PGO content. Notably, PBI-PGO 3:1 achieved a water sorption of 101%, already 1.5 times higher than pure PBI (66%). The performance regularly increased up to PBI-PGO 1:3, which guaranteed a 3.9 times enhancement thanks to final value of 257%. Such a behavior was a consequence of the hydrophilicity of the PGO sheets, which strengthened the water-holding ability of the composite membranes, a feature that could possibly facilitate proton transport as well [35,65–67].

The calculated long-term swelling ratios (SR) of the PBI-PGO A:B samples are provided in Fig. 3.8**b**. After 90 days, none of the manufactured materials suffered an excessive dimensional swelling, a characteristic that would be fundamental for the prevention of a deterioration of mechanical and structural resistance in a fuel cell assembly. In general, the variation of SR among the composite membranes remained quite restrained, possibly as a result of intermolecular interactions between the functional groups of PBI and PGO, which prevented excessive transversal expansion [25,28,52]. Slightly higher swelling ratios were recorded for PBI-PGO 1:2 and, primarily, PBI-PGO 1:3, for which a maximum value of 26.8 ± 15.0% was found. Nevertheless, this outcome should not be considered negative, since it remains in the same order of magnitude as the other samples. The best combination of the analyzed properties was observed for PBI-PGO 1:1, which exhibited a 204% water

Table 3.3
Average IEC values with corresponding standard deviations of pure PBI, PBI-PGO A:B composites, and pure PGO.

	PBI	PBI-PGO 3:1	PBI-PGO 2:1	PBI-PGO 1:1	PBI-PGO 1:2	PBI-PGO 1:3	PGO
Average IEC (meq g^{-1})	0.096 ± 0.012	0.160 ± 0.031	0.132 ± 0.035	0.256 ± 0.049	0.294 ± 0.088	0.532 ± 0.152	1.784 ± 0.181

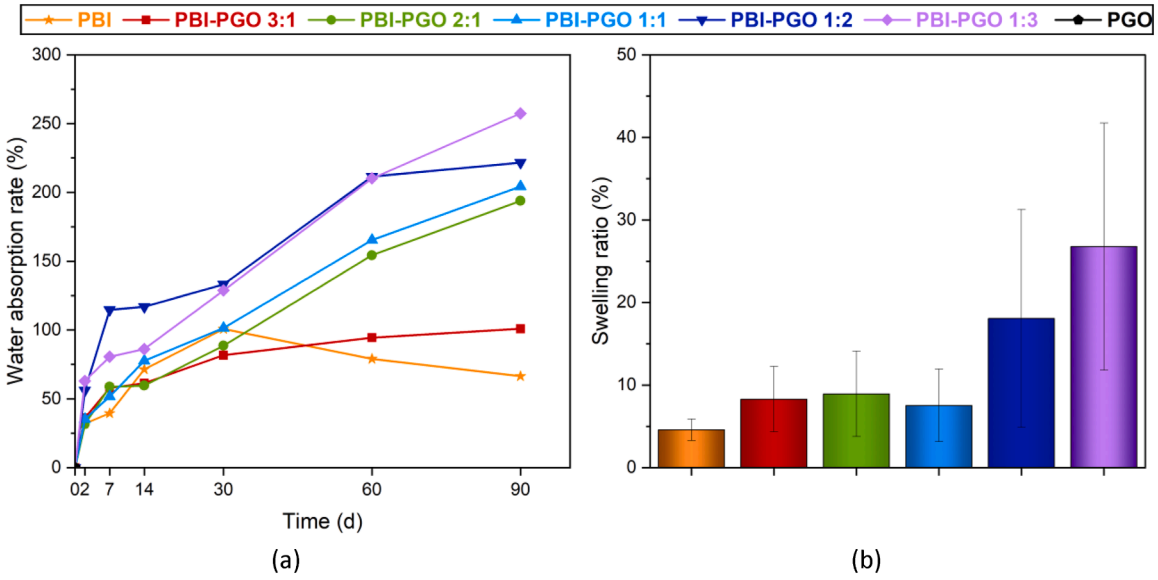

Fig. 3.8. Assessment of (a) water absorption rate and (b) swelling behavior of PBI-PGO A:B composite membranes, along with reference PBI and PGO.

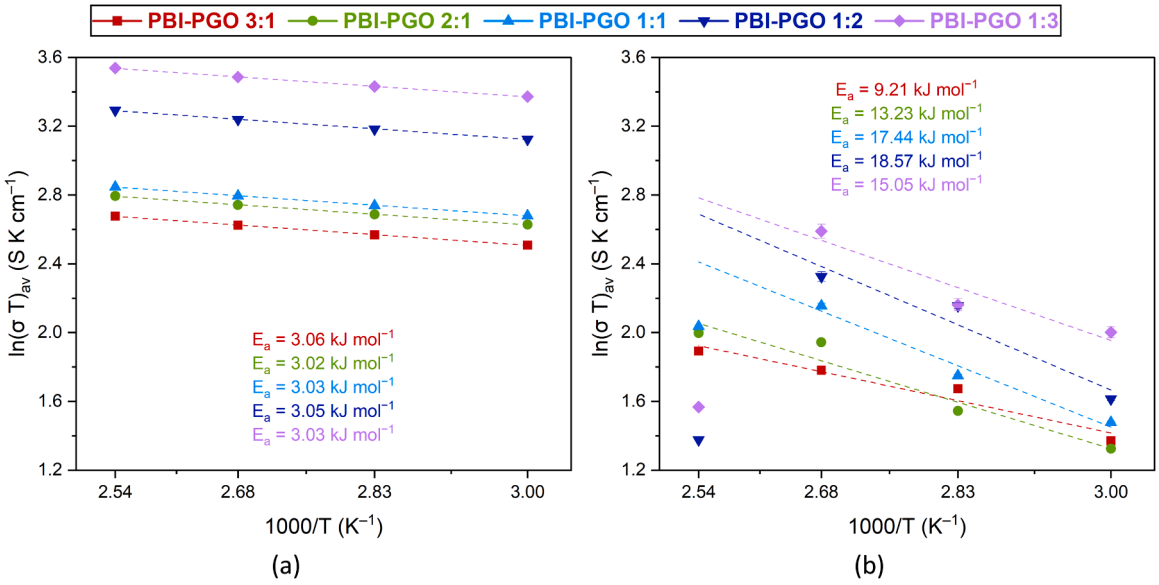

Fig. 3.9. Arrhenius plots of conductivity of PBI-PGO A:B samples in the 60–120 °C range for (a) in-plane and (b) through-plane configurations.

retention and the lowest swelling ratio of 7.5%.

3.4.3. *Electrochemical impedance spectroscopy*

The in-plane proton conductivities (σ_{IP}) of the PBI-PGO A:B composite membranes are collected in Figure 3.9**a** in the form of Arrhenius plots. An improvement at higher temperatures, due to the enhanced thermal activation of proton transport within the composite membranes and the consequently accelerated kinetics, can be inferred. This trend occurred since the energy barrier that hindered proton movement was more easily surpassed as the experimental temperature rose [27]. Furthermore, the proton conductivities of the undoped samples showcased a direct correlation with the PGO content, since the highest planar values were extrapolated for PBI-PGO 1:3 ($\sigma_{IP} = 0.088 \pm 5.7E\text{-}05$ S cm^{-1} at 120 °C), which not only demonstrated a 173% increase compared to pure PBI ($\sigma_{IP} = 0.032$ S cm^{-1} at 120 °C from a previous research [36]), but also a further 22% enhancement with respect to PBI-PGO 1:2 ($\sigma_{IP} = 0.068 \pm 1.3E\text{-}04$ at 120 °C). Several possible explanations could suit these findings, such as the sufficient acidity (pKa = 2–3) of the phosphonic acid groups (–PO_3H_2), which could facilitate the reception and release of protons [25,57,68], as well as the development of new routes for proton transport, occurring through the formation of a strong hydrogen bonding network among the amphoteric –PO_3H_2 functionalities and adjacent –NH– and –N═sites of the PBI chains [25,30]. Additionally, proton transfer may be emphasized across the amorphous microstructure, suggested by XRD patterns (Section 3.1.2), and by the reinforced water retention, which is aligned with the excellent behavior evidenced by the composite membranes through TGA results, even at 120 °C (Section 3.3.1) [25,64]. Coupling these factors with the restrained activation energies, all slightly superior than 3 kJ mol^{-1}, the Grotthuss mechanism can be identified as the dominant phenomenon in the in-plane direction [29,30]. The outcomes of the best performing sample, i.e., PBI-PGO 1:3, were mildly lower than those of commercial Nafion® at its working condition ($\sigma_{IP} = 0.12$ S cm^{-1} at 80 °C [7]), but they were positively achieved at higher temperatures (100–120 °C), at which the proton-carrying properties of the reference material start to fail. Moreover, the planar proton conductivity of PBI-PGO 1:3 at 120 °C

Table 3.4
Anisotropy factors of PBI-PGO A:B composite membranes at the temperatures assessed in the EIS measurements.

Anisotropy factor				
Temperature	**60 °C**	**80 °C**	**100 °C**	**120 °C**
PBI-PGO 3:1	0.51	0.42	0.40	0.37
PBI-PGO 2:1	0.57	0.52	0.38	0.38
PBI-PGO 1:1	0.54	0.46	0.31	0.39
PBI-PGO 1:2	0.64	0.47	0.43	0.74
PBI-PGO 1:3	0.59	0.56	0.42	0.76

surpassed the highest value reported for a PBI-GO composite membrane (0.046 S cm^{-1} with a 1:2 mass ratio [36]) in a previous work, highlighting the more suitable behavior of the formulation containing the phosphoric acid-functionalized variant.

The through-plane proton conductivities (σ_{TP}) of the PBI-PGO A:B composite membranes are displayed in Fig. 3.9**b.** Along with the boost associated with the gradual predominance of the PGO fraction, the rising trend due to temperature was confirmed up to 100 °C. Specifically, σ_{TP} grew from 0.016 ± 1.5E-0.5 S cm^{-1} for PBI-PGO 3:1 to 0.036 ± 1.7E-03 S cm^{-1} for PBI-PGO 1:3, highlighting an improvement equal to 125%. Considering the deduced values of activation energy, which ranged from 9.21 to 18.57 kJ mol^{-1}, a plausible larger contribution of the vehicular mechanism, more pronounced at lower temperatures, could be presumed [48,69]. The significant enhancement in water sorption capacity of the composite membranes with higher PGO concentration, discussed in Section 3.4.2, could be considered to support this consideration. However, when the operating temperature was 120 °C, the specimens with a PGO content higher than 50% underwent a conductivity reduction, probably resulting from the partial degradation of PGO sheets within the composite membranes or the reduced availability of useful water clusters. This drop may have been further exacerbated by the undesired loss of very labile oxygen-containing functional groups, which had previously facilitated water accumulation [36]. Nevertheless, a preliminary assessment of the stability of the through-plane proton conductivity carried out on six-month-aged composite membranes provided a promising outcome. In detail, the results (Figure S1, Supplementary Material) highlighted the almost complete retention of the original response, which could represent a positive feature in light of a future evaluation of the stability to repeated operating cycles.

The anisotropy factors as a function of the analyzed PBI-PGO mass ratios and temperature were calculated to examine the difference in the results derived from the two measurement configurations. This parameter is usually determined for Nafion®-based membranes [70], which can achieve values of 0.60–0.70 depending on the manufacturing process and preliminary treatments. The computed outcomes for the PBI-PGO A:B composite membranes, gathered in Table 3.4, ranged between 0.31 and 0.64, demonstrating a greater inclination for in-plane proton conductivity. Increased values with higher PGO content, and, hence, with lower thickness, were probably related to more marked interfacial effects that undermined the ability of protons to move transversally. Conversely, harsher temperature conditions were beneficial, since a higher thermal excitation tended to flatten the discrepancy between the performances in the in-plane and through-plane directions. The only exceptions were PBI-PGO 1:2 and PBI-PGO 1:3 at 120 °C, for which the abovementioned drop in through-plane proton conductivity caused their anisotropy factor (0.74 and 0.76, respectively) to diverge from the values of the other samples.

A comparison of the fundamental properties (peak stress, IEC, and proton conductivities) of PBI-PGO 1:2, PBI-PGO 1:3, and other non-fluorinated proton exchange membranes reported in the literature is displayed in Table 3.5. Notably, the experimental values discussed in the present study were comparable to, or in some cases even better than both the ones of PA-doped PBI-based membranes and composite membranes incorporating different materials. Such an observation was particularly significant, since the composite membranes developed in this work were never doped. In contrast, they relied on substantially higher loadings of PGO that are uncommon in the literature, where the same material is rarely employed as a filler in limited quantities. Altogether, the performances of PBI-PGO 1:2 and PBI-PGO 1:3 clarified the potential of these novel non-fluorinated composite membranes, especially in bridging the *"conductivity gap"* temperature range.

4. Conclusions

PBI-PGO composite membranes with various mass ratios were prepared through a lab-designed solution casting method and characterized with a view to the potential applicability in PEMFCs operating within the "*conductivity gap*" temperature range (80–120 °C). Different PBI to PGO mass ratios (3:1, 2:1, 1:1, 1:2, and 1:3), markedly different from the typical ones employed in the literature, were analyzed with the aim of avoiding the use of phosphoric acid doping to reach an acceptable proton conductivity. The morphological and microstructural characterization confirmed the successful formation of stable composite membranes. Smoother surfaces were noticed with a higher PBI content, while an increase in PGO amount led to a more wrinkled texture. The X-ray diffractograms revealed amorphous structures that might be favorable for proton conductivity. The EDS compositional analysis demonstrated the effective functionalization of GO and the preservation of the constitutive elements (C, N, O, P) in the prepared materials. TGA confirmed the ability of the membranes to maintain more than 90% of their mass at around 100 °C, with moisture release as the main loss. Mechanical testing revealed that both peak stress (up to 27.6 MPa) and Young's modulus (up to 3.4 GPa) increased with a PGO content up to 66.7 wt%. However, the maximum strain decreased, indicating a deterioration of the original deformability of PBI. The IEC trend suggested an effective blending, as the best values were reached by the 1:3 formulation. Moreover, the same sample demonstrated a 257% water uptake from immersion tests, an optimal long-term stability, and an acceptable swelling ratio (26.8%). The EIS analysis from 60 to 120 °C displayed

Table 3.5
Comparison of the properties of the composite membranes PBI-PGO 1:2 and PBI-PGO 1:3, produced in this study, and those of state-of-the-art materials reported in the literature.

Material	Peak stress (MPa)	IEC (meq g^{-1})	σ_{IP} (S cm^{-1})	σ_{TP} (S cm^{-1})	Anisotropy factor	Reference
PBI-SGO 1:2	/	0.25	0.113 (120 °C)	0.011 (120 °C)	0.83	[9]
PBI-GO 1:3	29.3	0.80	0.045 (100 °C)	/	/	[36]
PBI-SGO-0.5% (PA)	/	/	/	0.015 (130 °C)	/	[25]
PBI-PGO-0.5% (PA)	/	/	/	0.016 (130 °C)	/	[25]
Py-PBI/1.5% PGO/PA	7.14	/	0.060 (120 °C)	/	/	[30]
PBI/PGO-1.5%-PA	38.4	/	0.011 (120 °C)	/	/	[28]
PBI-GO 2% (PA)	/	/	0.065 (140 °C)	/	/	[47]
PBI@ZIF-mix (PA)	87.0	/	0.075 (120 °C)	/	/	[71]
SPEEK/SPOO-75%	11.5	1.69	0.100 (80 °C)	/	/	[72]
6PPMG	/	0.71	0.060 (80 °C)	/	/	[73]
PBI-PGO 1:2	27.6	0.29	0.068 (100 °C)	0.027 (100 °C)	0.43	This work
PBI-PGO 1:3	14.6	0.53	0.087 (100 °C)	0.036 (100 °C)	0.42	This work

proton conductivities approaching those of commercial electrolytes, but at temperatures included within the *"conductivity gap"* range. PGO mass contents exceeding 50 wt% facilitated the establishment of useful hydrogen bonded pathways, such that PBI-PGO 1:3 reached the best in-plane (0.088 S cm^{-1} at 120 °C) and through-plane (0.036 S cm^{-1} at 100 °C) proton conductivities. The associated anisotropy factors varied between 0.31 and 0.64, highlighting a tendency toward an efficient proton transport in both directions. Accordingly, the promising features demonstrated by the materials developed in this work, particularly at higher PGO mass content, underscored their potential as alternatives to currently used PFAS-containing proton exchange membranes, although future investigations will be crucial for a direct comparison in terms of long-term cycling stability and actual durability.

CRediT authorship contribution statement

Saverio Latorrata: Writing – review & editing, Supervision, Resources, Methodology, Conceptualization. **Matteo Di Virgilio:** Writing – original draft, Visualization, Data curation, Conceptualization, Investigation, Validation. **Matteo Andrea De Luca:** Writing – original draft, Investigation, Data curation, Validation. **Andrea Basso Peressut:** Writing – review & editing, Visualization, Methodology, Investigation, Validation.

Declaration of Competing Interest

The authors declare that they have no known competing financial interests or personal relationships that could have appeared to influence the work reported in this paper.

Appendix A. Supporting information

Supplementary data associated with this article can be found in the online version at doi:10.1016/j.nxmate.2026.101780.

References

[1] IEA | World energy outlook 2023, 1–355. https://www.iea.org/reports/world-energy-outlook-2023 (accessed July 21, 2025).

[2] United Nations, World Population Prospects 2024: Summary of Results (UN DESA/POP/2024/TR/NO. 9), United Nations, New York (NY, USA), 2024. ⟨https://population.un.org/wpp/assets/Files/WPP2024_Summary-of-Results.pdf⟩ (accessed July 21, 2025).

[3] The Paris agreement | UNFCCC,. ⟨https://unfccc.int/process-and-meetings/the-paris-agreement⟩ (accessed July 21, 2025).

[4] A.L. Dicks, D.A.J. Rand, Proton-exchange membrane fuel cells. Fuel Cell Syst. Explain., 3rd ed., John Wiley & Sons, Ltd, Chichester (UK), 2018, pp. 69–133, https://doi.org/10.1002/9781118706992.ch4.

[5] O.Z. Sharaf, M.F. Orhan, An overview of fuel cell technology: fundamentals and applications, Renew. Sustain. Energy Rev. 32 (2014) 810–853, https://doi.org/10.1016/j.rser.2014.01.012.

[6] R.S.L. Yee, R.A. Rozendal, K. Zhang, B.P. Ladewig, Cost effective cation exchange membranes: a review, Chem. Eng. Res. Des. 90 (2012) 950–959, https://doi.org/10.1016/j.cherd.2011.10.015.

[7] X. Sun, S.C. Simonsen, T. Norby, A. Chatzitakis, Composite membranes for high temperature PEM fuel cells and electrolysers: a critical review, Membr. (Basel) 9 (2019) 1–46, https://doi.org/10.3390/membranes9070083.

[8] S. Ahmad, T. Nawaz, A. Ali, M.F. Orhan, A. Samreen, A.M. Kannan, An overview of proton exchange membranes for fuel cells: materials and manufacturing, Int. J. Hydrog. Energy 47 (2022) 19086–19131, https://doi.org/10.1016/j.ijhydene.2022.04.099.

[9] M. Di Virgilio, A. Basso Peressut, S. Provato, S. Latorrata, Development and characterization of novel PBI/SGO composites as possible proton exchange membranes filling the "conductivity gap", J. Sci. Adv. Mater. Devices 9 (2024) 1–12, https://doi.org/10.1016/j.jsamd.2024.100767.

[10] D. Cai, Y. Zhou, B. Wang, Y. Ke, B. Xiao, L. Hu, Q. Liu, X. Fu, X. Li, K. Geng, N. Li, Mica ionogels-enhanced electrospun Nafion composite membranes: synergistic proton conduction and mechanical reinforcement for PEMFCs, J. Memb. Sci. 732 (2025) 1–9, https://doi.org/10.1016/j.memsci.2025.124260.

[11] A.N. García, N. Viciano, R. Font, Products obtained in the fuel-rich combustion of PTFE at high temperature, J. Anal. Appl. Pyrolysis 80 (2007) 85–91, https://doi.org/10.1016/j.jaap.2007.01.004.

[12] M. Di Virgilio, A. Basso Peressut, V. Arosio, A. Arrigoni, S. Latorrata, G. Dotelli, Functional and environmental performances of novel electrolytic membranes for PEM fuel cells: a lab-scale case study, Clean. Technol. 5 (2023) 74–93, https://doi.org/10.3390/cleantechnol5010005.

[13] R.A. Dickman, D.S. Aga, A review of recent studies on toxicity, sequestration, and degradation of per- and polyfluoroalkyl substances (PFAS), J. Hazard. Mater. 436 (2022) 1–14, https://doi.org/10.1016/j.jhazmat.2022.129120.

[14] M. Kim, H. Ko, S.Y. Nam, K. Kim, Study on control of polymeric architecture of sulfonated hydrocarbon-based polymers for high-performance polymer electrolyte membranes in fuel cell applications, Polym. (Basel) 13 (2021) 1–18, https://doi.org/10.3390/polym13203520.

[15] R.E. Rosli, A.B. Sulong, W.R.W. Daud, M.A. Zulkifley, T. Husaini, M.I. Rosli, E. H. Majlan, M.A. Haque, A review of high-temperature proton exchange membrane fuel cell (HT-PEMFC) system, Int. J. Hydrog. Energy 42 (2017) 9293–9314, https://doi.org/10.1016/j.ijhydene.2016.06.211.

[16] T. Li, S. Chai, B. Liu, C. Zhao, H. Li, All-carbon backbone aromatic polymers for proton exchange membranes, J. Polym. Sci. 61 (2023) 2796–2814, https://doi.org/10.1002/pol.20230405.

[17] M. Segale, T. Seadira, R. Sigwadi, T. Mokrani, G. Summers, A new frontier towards the development of efficient SPEEK polymer membranes for PEM fuel cell applications: a review, Mater. Adv. 5 (2024) 7979–8006, https://doi.org/10.1039/D4MA00628C.

[18] J. Escorihuela, J. Olvera-Mancilla, L. Alexandrova, L.F. del Castillo, V. Compañ, Recent progress in the development of composite membranes based on polybenzimidazole for high temperature proton exchange membrane (PEM) fuel cell applications, Polym. (Basel) 12 (2020) 1–41, https://doi.org/10.3390/polym12091861.

[19] A. Das, K.S. Im, M.M. Kabir, H.K. Shon, S.Y. Nam, Polybenzimidazole (PBI)-based membranes for fuel cell, water electrolysis and desalination, Desalination 579 (2024) 1–37, https://doi.org/10.1016/j.desal.2024.117500.

[20] B. Wang, Z. Ling, Q. Liu, X. Fu, R. Zhang, S. Hu, F. Zhao, X. Li, X. Bao, N. Li, J. Yang, Phosphoric acid-in-clay electrolyte boosting polybenzimidazole membranes for high-performance fuel cells, Adv. Funct. Mater. (2025) 1–13, https://doi.org/10.1002/adfm.202518482.

[21] A. Basso Peressut, S. Latorrata, P. Gallo Stampino, G. Dotelli, Development of self-assembling sulfonated graphene oxide membranes as a potential proton conductor, Mater. Chem. Phys. 257 (2021) 1–13, https://doi.org/10.1016/j.matchemphys.2020.123768.

[22] E. Quartarone, S. Angioni, P. Mustarelli, Polymer and composite membranes for proton-conducting, high-temperature fuel cells: a critical review, Mater. (Basel) 10 (2017) 1–17, https://doi.org/10.3390/ma10070687.

[23] D.R. Dreyer, S. Park, C.W. Bielawski, R.S. Ruoff, The chemistry of graphene oxide, Chem. Soc. Rev. 39 (2010) 228–240, https://doi.org/10.1039/B917103G.

[24] T. Bayer, S.R. Bishop, M. Nishihara, K. Sasaki, S.M. Lyth, Characterization of a graphene oxide membrane fuel cell, J. Power Sources 272 (2014) 239–247, https://doi.org/10.1016/j.jpowsour.2014.08.071.

[25] R.R.R. Sulaiman, R. Walvekar, W.Y. Wong, M. Khalid, M.M. Pang, Proton conductivity enhancement at high temperature on polybenzimidazole membrane electrolyte with acid-functionalized graphene oxide fillers, Membr. (Basel) 12 (2022) 1–23, https://doi.org/10.3390/membranes12030344.

[26] A. Abbasi, Y. Xu, E. Abouzari-Lotf, M. Etesami, R. Khezri, S. Risse, N. Kardjilov, K. Van Tran, H. Jia, A. Somwangthanaroj, I. Manke, Y. Lu, S. Kheawhom, Phosphonated graphene oxide-modified polyacrylamide hydrogel electrolytes for solid-state zinc-ion batteries, Electrochim. Acta 435 (2022) 1–11, https://doi.org/10.1016/j.electacta.2022.141365.

[27] A. Basso Peressut, M. Di Virgilio, A. Bombino, S. Latorrata, E. Muurinen, R. L. Keiski, G. Dotelli, Investigation of sulfonated graphene oxide as the base material for novel proton exchange membranes, Molecules 27 (2022) 1–19, https://doi.org/10.3390/molecules27051507.

[28] X. Zhao, B. Nan, Y. Lu, C. Zhao, S. Xu, Phosphorylated graphene oxide-reinforced polybenzimidazole composite membrane for high-temperature proton exchange membrane fuel cell, J. Polym. Res. 28 (2021) 1–15, https://doi.org/10.1007/s10965-021-02846-x.

[29] Y.N. Yusoff, K.S. Loh, W.Y. Wong, W.R.W. Daud, T.K. Lee, Sulfonated graphene oxide as an inorganic filler in promoting the properties of a polybenzimidazole membrane as a high temperature proton exchange membrane, Int. J. Hydrog. Energy 45 (2020) 27510–27526, https://doi.org/10.1016/j.ijhydene.2020.07.026.

[30] E. Abouzari-Lotf, M. Zakeri, M.M. Nasef, M. Miyake, P. Mozarmnia, N.A. Bazilah, N.F. Emelin, A. Ahmad, Highly durable polybenzimidazole composite membranes with phosphonated graphene oxide for high temperature polymer electrolyte membrane fuel cells, J. Power Sources 412 (2019) 238–245, https://doi.org/10.1016/j.jpowsour.2018.11.057.

[31] Z. Xu, N. Chen, S. Huang, S. Wang, D. Han, M. Xiao, Y. Meng, Strategies for mitigating phosphoric acid leaching in high-temperature proton exchange membrane fuel cells, Molecules 29 (2024) 1–34, https://doi.org/10.3390/molecules29184480.

[32] Y. Devrim, H. Devrim, I. Eroglu, Polybenzimidazole/SiO2 hybrid membranes for high temperature proton exchange membrane fuel cells, Int. J. Hydrog. Energy 41 (2016) 10044–10052, https://doi.org/10.1016/j.ijhydene.2016.02.043.

[33] R. Haider, Y. Wen, Z.-F. Ma, D.P. Wilkinson, L. Zhang, X. Yuan, S. Song, J. Zhang, High temperature proton exchange membrane fuel cells: progress in advanced materials and key technologies, Chem. Soc. Rev. 50 (2021) 1138–1187, https://doi.org/10.1039/D0CS00296H.

[34] A.A. Wani, N. Shaari, S.K. Kamarudin, N.F. Raduwan, Y.N. Yusoff, A.M. Khan, S. Yousuf, A. M, N. M., Critical review on composite-based polymer electrolyte membranes toward fuel cell applications: progress and perspectives, Energy Fuels 38 (2024) 18169–18193, https://doi.org/10.1021/acs.energyfuels.4c02516.

[35] J. Chen, Z. Guo, M. Perez-Page, Y. Jia, Z. Zhao, S.M. Holmes, Synthesis of phosphonated graphene oxide by electrochemical exfoliation to enhance the performance and durability of high-temperature proton exchange membrane fuel cells, J. Energy Chem. 76 (2023) 448–458, https://doi.org/10.1016/j.jechem.2022.09.028.
[36] M. Di Virgilio, A. Basso Peressut, A. Pontoglio, S. Latorrata, G. Dotelli, Study of innovative GO/PBI composites as possible proton conducting membranes for electrochemical devices, Membr. (Basel) 13 (2023) 428, https://doi.org/10.3390/membranes13040428.
[37] Y. Devrim, G.N. Bulanık Durmuş, Composite membrane by incorporating sulfonated graphene oxide in polybenzimidazole for high temperature proton exchange membrane fuel cells, Int. J. Hydrog. Energy 47 (2022) 9004–9017, https://doi.org/10.1016/j.ijhydene.2021.12.257.
[38] M. Acik, G. Lee, C. Mattevi, A. Pirkle, R.M. Wallace, M. Chhowalla, K. Cho, Y. Chabal, The role of oxygen during thermal reduction of graphene oxide studied by infrared absorption spectroscopy, J. Phys. Chem. C. 115 (2011) 19761–19781, https://doi.org/10.1021/jp2052618.
[39] E. Moukheiber, G. De Moor, L. Flandin, C. Bas, Investigation of ionomer structure through its dependence on ion exchange capacity (IEC), J. Memb. Sci. 389 (2012) 294–304, https://doi.org/10.1016/j.memsci.2011.10.041.
[40] M. Vinothkannan, R. Kannan, A.R. Kim, G.G. Kumar, K.S. Nahm, D.J. Yoo, Facile enhancement in proton conductivity of sulfonated poly(ether ether ketone) using functionalized graphene oxide - Synthesis, characterization, and application towards proton exchange membrane fuel cells, Colloid Polym. Sci. 294 (2016) 1197–1207, https://doi.org/10.1007/s00396-016-3877-8.
[41] K. Feng, B. Tang, P. Wu, Evaporating" graphene oxide sheets (GOSs) for rolled up GOSs and its applications in proton exchange membrane fuel cell, ACS Appl. Mater. Interfaces 5 (2013) 1481–1488, https://doi.org/10.1021/am302995c.
[42] X.-Z. Yuan, C. Song, H. Wang, J. Zhang, Impedance and its corresponding electrochemical processes. Electrochem. Impedance Spectrosc. PEM Fuel Cells, Springer London, London (UK), 2010, pp. 95–138, https://doi.org/10.1007/978-1-84882-846-9_3.
[43] X. Luo, G. Lau, M. Tesfaye, C.R. Arthurs, I. Cordova, C. Wang, M. Yandrasits, A. Kusoglu, Thickness dependence of proton-exchange-membrane properties, J. Electrochem. Soc. 168 (2021) 1–18, https://doi.org/10.1149/1945-7111/ac2973.
[44] A. Figoli, T. Marino, S. Simone, E. Di Nicolò, X.-M. Li, T. He, S. Tornaghi, E. Drioli, Towards non-toxic solvents for membrane preparation: a review, Green. Chem. 16 (2014) 1–26, https://doi.org/10.1039/C4GC00613E.
[45] K.Y. Wang, M. Weber, T.-S. Chung, Polybenzimidazoles (PBIs) and state-of-the-art PBI hollow fiber membranes for water, organic solvent and gas separations: a review, J. Mater. Chem. A. 10 (2022) 8687–8718, https://doi.org/10.1039/D2TA00422D.
[46] K. Bozkurt, L. Akyalçın, S. Kjelstrup, The thermal diffusion coefficient of membrane-electrode assemblies relevant to polymer electrolyte membrane fuel cells, Int. J. Hydrog. Energy 48 (2023) 1501–1513, https://doi.org/10.1016/j.ijhydene.2022.09.302.
[47] S. Diaz-Abad, S. Fernández-Mancebo, M.A. Rodrigo, J. Lobato, Characterization of PBI/graphene oxide composite membranes for the SO2 depolarized electrolysis at high temperature, Membr. (Basel) 12 (2022) 1–13, https://doi.org/10.3390/membranes12020116.
[48] N. Üregen, K. Pehlivanoğlu, Y. Özdemir, Y. Devrim, Development of polybenzimidazole/graphene oxide composite membranes for high temperature PEM fuel cells, Int. J. Hydrog. Energy 42 (2017) 2636–2647, https://doi.org/10.1016/j.ijhydene.2016.07.009.
[49] A.C. Reynosa-Martínez, E. Gómez-Chayres, R. Villaurrutia, E. López-Honorato, Controlled reduction of graphene oxide using sulfuric acid, Mater. (Basel) 14 (2020) 1–10, https://doi.org/10.3390/ma14010059.
[50] B. Wang, Z. Ling, N. Li, Q. Liu, X. Fu, R. Zhang, S. Hu, Z. Meng, F. Zhao, X. Li, Graphene oxide-intercalated montmorillonite layered stack incorporated into poly (2,5-benzimidazole) for preparing wide-temperature proton exchange membranes, ACS Appl. Nano Mater. 6 (2023) 20355–20366, https://doi.org/10.1021/acsanm.3c04409.
[51] C. Xu, Y. Cao, R. Kumar, X. Wu, X. Wang, K. Scott, A polybenzimidazole/sulfonated graphite oxide composite membrane for high temperature polymer electrolyte membrane fuel cells, J. Mater. Chem. 21 (2011) 1–6, https://doi.org/10.1039/c1jm11159k.
[52] S. Gao, X. Chen, H. Xu, T. Luo, A. Ouadah, Z. Fang, Y. Li, R. Wang, C. Jing, C. Zhu, Sulfonated graphene oxide-doped proton conductive membranes based on polymer blends of highly sulfonated poly(ether ether ketone) and sulfonated polybenzimidazole, J. Appl. Polym. Sci. 135 (2018) 1–11, https://doi.org/10.1002/app.46547.
[53] S. Changkhamchom, A. Sirivat, Sulfonated (graphene oxide/poly(ether ketone ether sulfone) (S-GO/S-PEKES) composite proton exchange membrane with high proton conductivity for direct methanol fuel cell, Polym. Technol. Mater. 58 (2019) 1900–1913, https://doi.org/10.1080/25740881.2019.1587770.
[54] T. Bayer, B.V. Cunning, R. Selyanchyn, T. Daio, M. Nishihara, S. Fujikawa, K. Sasaki, S.M. Lyth, Alkaline anion exchange membranes based on KOH-treated multilayer graphene oxide, J. Memb. Sci. 508 (2016) 51–61, https://doi.org/10.1016/j.memsci.2016.02.017.
[55] M.U. Khan, M.A. Shaida, Reduction mechanism of graphene oxide including various parameters affecting the C/O ratio, Mater. Today Commun. 36 (2023) 1–28, https://doi.org/10.1016/j.mtcomm.2023.106577.
[56] R.K. Singh, R. Kumar, D.P. Singh, Graphene oxide: strategies for synthesis, reduction and frontier applications, RSC Adv. 6 (2016) 64993–65011, https://doi.org/10.1039/C6RA07626B.
[57] X. Li, X. Chen, B.C. Benicewicz, Synthesis and properties of phenylindane-containing polybenzimidazole (PBI) for high-temperature polymer electrolyte membrane fuel cells (PEMFCs), J. Power Sources 243 (2013) 796–804, https://doi.org/10.1016/j.jpowsour.2013.06.033.
[58] Y. Kang, J. Zou, Z. Sun, F. Wang, H. Zhu, K. Han, W. Yang, H. Song, Q. Meng, Polybenzimidazole containing ether units as electrolyte for high temperature proton exchange membrane fuel cells, Int. J. Hydrog. Energy 38 (2013) 6494–6502, https://doi.org/10.1016/j.ijhydene.2013.03.051.
[59] P.A. Christensen, S.W.M. Jones, An in situ FTIR study of undoped PolyBenzoImadazole as a function of relative humidity, Polym. Degrad. Stab. 105 (2014) 211–217, https://doi.org/10.1016/j.polymdegradstab.2014.04.020.
[60] F.H. Akhtar, M. Kumar, L.F. Villalobos, H. Vovusha, R. Shevate, U. Schwingenschlögl, K.-V. Peinemann, Polybenzimidazole-based mixed membranes with exceptionally high water vapor permeability and selectivity, J. Mater. Chem. A. 5 (2017) 21807–21819, https://doi.org/10.1039/C7TA05081J.
[61] X. Tian, S. Wang, J. Li, F. Liu, X. Wang, H. Chen, D. Wang, H. Ni, Z. Wang, Benzimidazole grafted polybenzimidazole cross-linked membranes with excellent PA stability for high-temperature proton exchange membrane applications, Appl. Surf. Sci. 465 (2019) 332–339, https://doi.org/10.1016/j.apsusc.2018.09.170.
[62] S. Eigler, C. Dotzer, A. Hirsch, M. Enzelberger, P. Müller, Formation and decomposition of CO2 intercalated graphene oxide, Chem. Mater. 24 (2012) 1276–1282, https://doi.org/10.1021/cm203223z.
[63] Y.-J. Kuo, H.-L. Lin, Effects of mesoporous fillers on properties of polybenzimidazole composite membranes for high-temperature polymer fuel cells, Int. J. Hydrog. Energy 43 (2018) 4448–4457, https://doi.org/10.1016/j.ijhydene.2017.12.128.
[64] Z. Meng, Y. Zou, N. Li, B. Wang, X. Fu, R. Zhang, S. Hu, X. Bao, X. Li, F. Zhao, Q. Liu, Graphene oxide-intercalated microbial montmorillonite to moderate the dependence of Nafion-based PEMFCs in high-humidity environments, ACS Appl. Energy Mater. 6 (2023) 1771–1780, https://doi.org/10.1021/acsaem.2c03666.
[65] X. He, G. He, A. Zhao, F. Wang, X. Mao, Y. Yin, L. Cao, B. Zhang, H. Wu, Z. Jiang, Facilitating proton transport in Nafion-based membranes at low humidity by incorporating multifunctional graphene oxide nanosheets, ACS Appl. Mater. Interfaces 9 (2017) 27676–27687, https://doi.org/10.1021/acsami.7b06424.
[66] F.B. Baz, R.M. Elzohary, S. Osman, S.A. Marzouk, M. Ahmed, A review of water management methods in proton exchange membrane fuel cells, Energy Convers. Manag. 302 (2024) 1–30, https://doi.org/10.1016/j.enconman.2024.118150.
[67] G. Shukla, R.P. Pandey, V.K. Shahi, Temperature resistant phosphorylated graphene oxide-sulphonated polyimide composite cation exchange membrane for water desalination with improved performance, J. Memb. Sci. 520 (2016) 972–982, https://doi.org/10.1016/j.memsci.2016.08.050.
[68] M. Schaffer, T. Licha, A guideline for the identification of environmentally relevant, ionizable organic molecule species, Chemosphere 103 (2014) 12–25, https://doi.org/10.1016/j.chemosphere.2013.12.009.
[69] F.C. Teixeira, A.I. de Sá, A.P. S, C.M. Teixeira, Rangel, Nafion phosphonic acid composite membranes for proton exchange membranes fuel cells, Appl. Surf. Sci. 487 (2019) 889–897, https://doi.org/10.1016/j.apsusc.2019.05.078.
[70] S. Shi, A.Z. Weber, A. Kusoglu, Structure/property relationship of Nafion XL composite membranes, J. Memb. Sci. 516 (2016) 123–134, https://doi.org/10.1016/j.memsci.2016.06.004.
[71] J. Escorihuela, Ó. Sahuquillo, A. García-Bernabé, E. Giménez, V. Compañ, Phosphoric acid doped polybenzimidazole (PBI)/zeolitic imidazolate framework composite membranes with significantly enhanced proton conductivity under low humidity conditions, Nanomaterials 8 (2018) 1–13, https://doi.org/10.3390/nano8100775.
[72] M.I. Khan, A. Shanableh, S. Shahida, M.H. Lashari, S. Manzoor, J. Fernandez, SPEEK and SPPO blended membranes for proton exchange membrane fuel cells, Membr. (Basel) 12 (2022) 1–12, https://doi.org/10.3390/membranes12030263.
[73] S. Ahmed, F. Altaf, S.A. Khan, S. Manzoor, A. Ahmad, M. Mansha, S. Ali, Ata-ur-Rehman, K. Jacob, Probing the efficiency of PPMG-based composite electrolytes for applications of proton exchange membrane fuel cell, Trans. Tianjin Univ. 30 (2024) 262–283, https://doi.org/10.1007/s12209-024-00396-z.